Sustainable Energy & Fuels

ROYAL SOCIETY OF CHEMISTRY

PAPER

View Article Online
View Journal | View Issue

Cite this: *Sustainable Energy Fuels*, 2026, **10**, 227

Bifunctional PGM-free electrocatalysts for seawater batteries

Pedro Pablo Machado Pico,[a] Jorge Montero,[a] Akiko Tsurumaki, *[ad] Stefano Passerini [bc] and Maria Assunta Navarra *[ad]

Received 29th June 2025
Accepted 23rd October 2025

DOI: 10.1039/d5se00907c

rsc.li/sustainable-energy

Seawater batteries (SWBs) are an emerging energy storage solution that leverages the abundant and cost-effective sodium ions present in seawater. However, their performance is often constrained by the sluggish kinetics of the oxygen evolution reaction (OER) and oxygen reduction reaction (ORR) at the seawater cathode. To overcome these limitations, a series of platinum group metal (PGM)-free bifunctional electrocatalysts was developed to enhance OER/ORR catalytic activity and overall power performance. Metal-doped nitrogen carbon nanoparticles (M–N–C), namely FeNiNC, FeNC, and NiNC, were synthesized *via* a simple precipitation method followed by heat treatment, yielding active metal sites dispersed in an amorphous carbon structure. The use of low-cost biomass derived from hazelnut shells as a carbon-based material, modified with Fe and/or Ni, resulted in a highly efficient catalyst. In particular, FeNiNC exhibited an ORR activity of 0.81 V *vs.* RHE at half-potential and an OER activity of 1.57 V *vs.* RHE at a current density of 10 mA cm^{-2}. Electrochemical characterization demonstrated that SWBs incorporating the FeNiNC catalyst achieved enhanced power output and cycling stability, maintaining performance for 350 hours.

Introduction

Rechargeable seawater batteries (SWBs) are innovative and promising sustainable energy storage devices, primarily due to the abundance and renewability of their cathode material, *i.e.*, seawater. The system operates utilizing Na^+ ions and hydroxide OH^- ions present in seawater. During charging, sodium ions gain electrons from the cathode, where O_2 is formed through the oxygen evolution reaction (OER). Conversely, during discharge, dissolved O_2 in seawater is reduced back to OH^- *via* the oxygen reduction reaction (ORR).[1] Theoretically, the OER and ORR occur at approximately 3.4 V *vs.* Na/Na^+ in nearly pH-neutral seawater (pH ≈ 8).[2] While this OER/ORR mechanism offers the advantages of seawater, an abundant and renewable cathode material, the slow kinetics of these reactions result in significant overpotentials during operation. In typical seawater battery setups, where carbon paper is immersed in seawater, the potential plateaus for the OER and ORR appear at 3.9 V and 2.8 V *vs.* Na/Na^+, respectively.[3] This large overpotential highlights the need for efficient bifunctional electrocatalysts to enhance reaction kinetics.[4]

The most commonly used catalysts for the ORR and OER are based on platinum group metals (PGMs), with Pt and IrO_2/RuO_2 being the standard choices for these reactions, respectively. However, the limited availability and high cost of PGM catalysts pose significant barriers to the commercial viability of devices relying on these reactions, including SWBs.[5] The first PGM-free catalysts explored for SWBs were cobalt manganese oxides (CMOs), synthesized through the pyrolysis of a Prussian blue analogue, $Mn_3[Co(CN)_6]_2 \cdot nH_2O$. The SWBs employing CMO demonstrated a relatively small voltage gap of approximately 0.53 V, which is notably lower than the gaps observed with commercial Pt/C (~0.64 V) and Ir/C (~0.73 V) catalysts and much smaller than that of SWBs without any catalyst (~1.05 V).[3]

The ORR proceeds *via* two main pathways: a two-electron transfer forming H_2O_2/HO_2^- and a four-electron transfer producing H_2O/OH^-. The latter pathway is preferred due to its faster kinetics.[6,7] Various families of PGM-free catalysts have been studied for ORR catalysis, including spinels,[3,8] perovskites,[9] and metal–organic frameworks.[10] For the OER, the performance is constrained by the formation of multiple intermediates, from OH^- to O_2. Optimizing OER catalysts involves regulating the binding energies of these reactive intermediates, thereby improving the adsorption and desorption processes of OH^- and O_2.[11] Several catalyst families, including metal alloys,[12,13] phosphides,[14] and chalcogenides,[15] have been studied to enhance OER kinetics.

[a]*Department of Chemistry, Sapienza University of Rome, P.le Aldo Moro 5, Rome, 00185, Italy. E-mail: akiko.tsurumaki@uniroma1.it; mariassunta.navarra@uniroma1.it*

[b]*KIT Campus Transfer GmbH, Haid-und-Neu-Str.7, 76131 Karlsruhe, Germany*

[c]*Austrian Institute of Technology (AIT), Center for Transport Technologies, Giefinggasse 2, 1210 Vienna, Austria*

[d]*Hydro-Eco Research Center, Sapienza University of Rome, Via A. Scarpa 16, Rome, 00161, Italy*

Among PGM-free materials, metal–nitrogen–carbon (M–N–C) catalysts are the most prominent due to their high ORR activity and strong tolerance to contaminants.[16] These electrocatalysts contain diverse catalytic sites, including pyrrolic, pyridinic, and M–N_x configurations,[17] where the coordination of metal atoms to nitrogen atoms enhances the direct four-electron reduction of oxygen to water.[18,19] N-doping of carbon substrates is essential for stabilizing transition metal coordination, maintaining a high density of M–N_x active sites, and preventing catalyst aggregation.[20] Among various metal precursors, iron(II) phthalocyanine has gained particular interest for the synthesis of Fe–N–C catalysts owing to its low cost, tunable electronic structure, facile synthesis, and low ORR overpotential.[21,22] Moreover, incorporating Fe with secondary metals such as Ni or Co is advantageous for OER catalysis, as the modification of the 3d orbital structure increases metal–O covalency.[23] In this bimetallic context, Fe–N_x moieties act as dominant active sites for the ORR by facilitating O_2 adsorption and accelerating the first electron transfer to form OOH* intermediates, thereby reducing the energy barrier of the rate-determining step. In contrast, Ni centers contribute to the OER by stabilizing high-valence Ni^{3+}/Ni^{4+} species during anodic polarization, promoting both the formation and deprotonation of OOH* intermediates. The close spatial proximity of Fe–N and Ni–N sites further enhances electron redistribution and optimizes intermediate binding energies, effectively lowering the energy barriers for OOH* generation and decomposition in both reaction pathways.[24–26]

To emphasize the sustainable feature of SWBs, biomass-derived carbon materials are highly suitable due to their eco-friendliness, abundance, and renewability as well as other properties suitable for electrodes such as high specific surface area, desirable electrical conductivity, tuneable porosity (micro, meso, and macro), and excellent thermal and chemical stability. N-doped carbon derived from biomass improves electrical conductivity, enhances electron–donor properties, expands the graphite layer spacing, increases the number of electroactive sites, and generates defect sites that provide ample space for electrolyte ions, thereby enhancing electrochemical reactivity and energy storage performance. Moreover, nitrogen self-doping has been reported to improve structural stability while tuning electronic properties and electrochemical activity.[27,28] In this context, a one-step pyrolysis treatment of biomass doped with a nitrogen source offers a simple, cost-effective, and eco-friendly approach for producing N-doped biochar. This method not only efficiently uses the carbon content of biomass, but also enhances its electrochemical properties for various energy storage and conversion applications.[29–32]

In this work, we developed a synthesis strategy to prepare an FeNi–N–C bifunctional catalyst through wet impregnation followed by pyrolysis. The metal precursors consisted of iron(II) phthalocyanine and nickel(II) phthalocyanine, while urea served as both the nitrogen and additional metal-coordination source. Functionalized biochar was employed as a conductive carbon support. Within this structure, Fe sites act as the primary catalytically active centers, whereas Ni sites modulate the local coordination environment, thereby optimizing the adsorption and desorption of oxygen intermediates.[33] The synthesized bifunctional FeNi–N–C catalyst was integrated into SWBs, showing desirable catalytic performance arising from the synergistic interplay between Fe and Ni species coordinated to nitrogen within the carbon matrix.

Materials and methods

Materials

Iron(II) phthalocyanine (FePc, Sigma-Aldrich), nickel(II) phthalocyanine (NiPc, Sigma), CH_4N_2O (urea, VWR Chemicals), ethanol (VWR Chemicals), isopropanol (Sigma-Aldrich), dimethylacetamide (DMA, Sigma-Aldrich), Nafion (5 wt% in lower aliphatic alcohols and water, Ion Power), diethylene glycol dimethyl ether (DEGDME, Sigma-Aldrich), biphenyl (BP, Sigma-Aldrich), activated carbon cloth (CC, Kynol), and Pt/C-RuO_2 (ElectroChem, Inc.) were purchased and used without purification.

Carbon support and catalyst preparation

Synthesis of the carbon support: Hazelnut shells were ball-milled in a Zirconia jar ($V = 500$ mL) with 100 Zirconia balls (10-mm diameter) in a planetary ball-mill (Pulverisette 6, Fritsch GmbH) for 6 h (45 min of milling with a 15 min pause) at a rotation rate of 400 rpm. Subsequently, 40 mg of the milled hazelnut powder and 160 mg of urea were mixed using a mortar and then pyrolyzed at different temperatures (700 or 900 °C) for 1 h under an Ar atmosphere, yielding two samples labelled as NC7 and NC9 according to the temperature values.

Preparation of M–N–C catalysts: 100 mg of FePc and 100 mg of NiPc were mixed using a mortar for 10 min followed by stirring overnight in 50 mL of DMA. The solution was dried at 80 °C to obtain an FeNi compound. The obtained FeNi powder (100 mg) and NC7 powder were mixed by hand using a mortar for 30 min, and then pyrolyzed in an Al_2O_3-tube furnace at 900 °C for 1 h under an Ar atmosphere, obtaining a sample labelled as FeNiNC. The FeNC and NiNC were prepared using the same preparation as FeNiNC by using either FePc or NiPc.

Catalyst ink preparation for the RDE: the catalyst ink was prepared by dispersing 5 mg of the catalyst in 985 μL of Milli-Q water and 15 μL of isopropanol mixture. This dispersion was treated in an ultrasonic bath at 60 Hz for 45 min. Then, 15 μL of Nafion solution was added to the dispersion, and further treated in the ultrasonic bath for 15 min. The ink was dropped (10 μL) onto a working electrode (glassy carbon rotating disk electrode (RDE), area = 0.247 cm^2, Pine Research Instrumentation), resulting in a catalyst loading of 0.2 mg cm^{-2}. Before use, the modified RDE was dried in a convection oven at 40 °C for 4 mins.

Seawater battery configuration

Preparation of the NaBP/DEGDME anolyte: DEGDME was dried over molecular sieves (4 Å, 8–12 mesh) for three days. Subsequently, BP was added into the dried DEGDME solvent to obtain a 1 M solution. The 1 M BP-DEGDME solution was stirred until complete dissolution, then Na metal was added to the solution

to obtain a concentration of 1.1 M in sodium. After stirring for 2 h a dark blue solution of NaBP/DEGDME was obtained.

Cathode preparation: a total of 25 mg of FeNiNC was added to 2 mL of ethanol and stirred for 30 minutes. Then, 970 μL of Nafion (5 wt% dispersion) were added to the solution, followed by continuous stirring for an additional 30 minutes. The resulting ink was applied *via* spray coating to a 4 × 4 cm CC placed on a hot plate at 50 °C. Reference electrodes containing Pt/C-RuO_2 were prepared using the same procedure. In all cases, the final catalyst loading was *ca.* 2 mg cm^{-2}. This value was chosen because it provides a good balance between ensuring sufficient active sites for catalytic activity, maintaining favorable mass transfer, and avoiding underutilization of the inner catalyst layer.[34]

SWB assembly: 2465-type coin cells with a NASICON ($Na_3Zr_2Si_2PO_{12}$) window, purchased from 4 TO ONE, were assembled using a disc of Nickel foam that worked as an anodic current collector, embedded with a NaBP/DEGDME solution as the anolyte in a glovebox. The sealed coin cells were immersed in artificial seawater comprising 0.47 M NaCl. To the same seawater, a CC cathode coated with Pt/C-RuO_2 or FeNiNC catalyst was immersed as the positive electrode. These seawater flow cell testers were also purchased from 4 TO ONE.

Microstructural characterization

The catalyst surface morphology was investigated using a Thermo Fisher Scientific Phenom ProX desktop scanning electron microscope equipped with energy dispersive spectroscopy (SEM-EDS) and high-resolution transmission electron microscope (HR-TEM) JEOL F-200 assembled with a GATAN Rio16 CMOS acquisition camera and a JEOL EDX spectrometer. Brunauer–Emmett–Teller (BET) analysis was conducted using a BELSORP MAX G from Microtrac to determine surface area and pore size distribution.

Raman spectroscopy was conducted using a Dilor Labram instrument equipped with a He–Ne laser source at 632.7 nm and a cooled CCD detector, which was calibrated with Si as the standard. The spectra were fitted using the Voigt function implemented in the origin lab.

Electrochemical measurements

Voltammetry: the catalytic activity toward the ORR and OER of the modified RDEs was examined by two steps: (1) cyclic voltammetry (CV) for both activation and preliminary evaluation and (2) linear sweep voltammetry (LSV) for precise evaluation, using a VMP Multichannel Potentiostat. A conventional three electrode cell was used. The reference electrode was Ag/AgCl (AMEL 303/SCG/12), the auxiliary electrode was a graphite rod, and the glassy carbon RDE modified with the catalyst layer served as a working electrode (see a former section for the preparation). CV was carried out at 10 mV s^{-1} without RDE rotation in either N_2- or O_2-saturated aqueous 0.1 M KOH solution; prior to the measurements, the electrodes were activated by performing 100 and 50 CV cycles at 500 and 20 mV s^{-1}, respectively.

To assess ORR and OER activity, LSV-RDE experiments were carried out at a scan rate of 10 mV s^{-1} and electrode rotation speed of 1600 rpm. The electrode potential was measured *vs.* Ag/AgCl and then converted to the reversible hydrogen electrode (RHE) scale, according to eqn (1):

$$E_{RHE} = E_{Ag/AgCl} + E^0_{Ag/AgCl} + 0.0591\ pH \quad (1)$$

where $E^0_{Ag/AgCl} = 0.197$ V.

Galvanostatic charge–discharge: cycling of SWBs was carried out at a current density of 0.3 mA cm^{-2} (cut-off 2 mA h) with voltage limits of 4.0 V *vs.* Na^+/Na for charge and 2.5 V *vs.* Na^+/Na for discharge.

Results and discussion

Materials characterization

The influence of thermal treatment temperature on hazelnut shell-derived carbon materials, namely, NC7 and NC9, as well as the effect of urea addition (C7) were studied as summarized in the supplementary information (Fig. S1a–f: SEM images and S1g: key elemental composition). Pore formation was not observed in the sample prepared without urea at 700 °C (Fig. S1a and d). In contrast, when urea was added, distinct holes and cracks appeared on the surfaces of NC7 (Fig. S1b and e) and NC9 (Fig. S1c and f), confirming that urea addition promotes pore formation, as previously reported in the literature.[35] Elemental analysis was conducted using EDS as summarized in S1g, showing an increase in C content and decrease in O and N contents at a higher temperature, *i.e.*, 900 °C. Increasing the carbonization temperature generally promotes a higher degree of graphitization and enhances porosity.[36] However, this improvement occurs at the expense of nitrogen retention, as many nitrogen-containing functional groups like pyridinic and pyrrolic species, which are considered the most catalytically active, tend to decompose at elevated temperatures.[37–40]

Enhanced porosity of NC7 and NC9, with respect to C7, was also confirmed by BET analysis. As shown in Fig. S2, the N_2 adsorption/desorption isotherms of all samples exhibit type I behavior, which is characteristic of microporous materials with pore sizes smaller than 2 nm.[41,42] Quantitative analysis revealed that the specific surface area of the urea-undoped C7 was 46.96 $m^2\ g^{-1}$, while urea doping significantly increased the surface area to 397.93 $m^2\ g^{-1}$ for NC7 and 405.37 $m^2\ g^{-1}$ for NC9. Considering the similar porous structures of NC7 and NC9, together with a slightly higher proportion of catalytically active nitrogen functionalities and a lower energy requirement for NC7 synthesis, NC7 was selected as the nitrogen–carbon support for subsequent studies, offering advantages in both catalytic performance and sustainability.

Employing the selected NC7 (hereafter referred to as NC), the bifunctional catalyst FeNiNC was synthesized. The surface area further increased to 419.44 $m^2\ g^{-1}$ for the FeNiNC composite, which is in good agreement with previous reports on FeNi–N–C electrocatalysts.[43–45] SEM-EDX mapping of the FeNiNC samples, reported in Fig. 1 and Table S2, confirmed the presence of C, N,

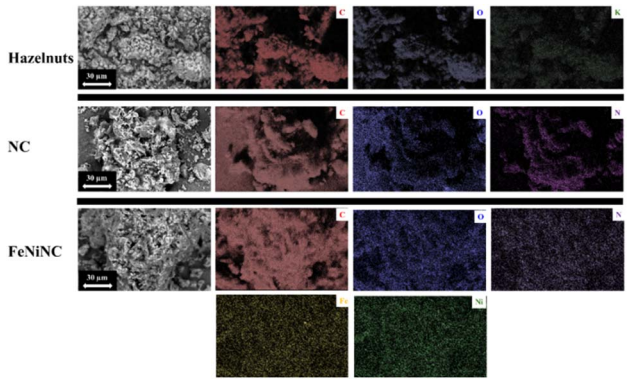

Fig. 1 SEM-EDS elemental mapping images of ball-milled hazelnut shells, NC formed at 700 °C and the final FeNiNC catalyst.

O, K, Ni, and Fe in both the precursor and the final catalyst. The presence of K originates from the pristine hazelnut sample (see Table S2). Upon introducing Fe and Ni to form FeNiNC, the concentration of C and O increased, while that of N decreased, likely due to partial loss of N species at elevated temperatures. EDS mapping images of Fe and Ni (Fig. 1) verify the uniform distribution of metal species across the biochar surface, with no significant agglomeration observed.

As shown in Fig. 2a, the Raman spectra of the catalysts were collected to assess the degree of graphitization of the carbon substrate. Generally, the intensity ratio of the D to G bands (I_D/I_G) serves as an indicator of graphitization. Among the various sp^2-hybridized forms of carbon, the D-band at 1350 cm^{-1} corresponds to defects in the amorphous carbon structure, while the G-band at 1580 cm^{-1} stands for the tangential vibration of sp^2-bonded carbon atoms. The intensity ratio between the D and G bands remained nearly identical for the FeNiNC catalyst and the monometallic catalysts, indicating that the introduction of metal did not significantly alter the graphitization degree of the carbon support.

The crystal structure of catalysts was investigated by XRD measurement. As shown in Fig. 2b, all three samples show the typical broad diffraction peak at 25.8° of the (002) lattice plane of graphitic carbon, indicating the occurrence of partial graphitization. For the NiNC sample, the peaks at 44.5°, 51.8°, and 76.3° can be assigned to Ni (JCPDS #04-0850) and those at 37.2°, 43.3°, and 75.4° to NiO (JCPDS #47-1049). The peaks associated with NiO are weaker than those of Ni, indicating that Ni is mostly present in its metallic form. In contrast, Fe is predominantly present in the oxidized form in FeNC as evidenced by the strong diffraction peaks at 30°, 35°, 43.5°, 53.9°, 57.5° and 63.1° corresponding to γ-Fe_2O_3 (JCPDS #65-3107) along with a weak signal at 44.3° attributed to metallic Fe (JCPDS #06-0696). The FeNiNC sample shows three distinct diffraction peaks at 44.1°, 51.4°, and 75.6° indexed to the (111), (200), and (220) crystal faces of the FeNi alloy (JCPDS no. 38-0419) in addition to the minor features due to γ-Fe_2O_3.

In addition, HR-TEM and EDX analyses were performed to gain deeper insights into the FeNiNC sample (Fig. S3). The HR-TEM images revealed the formation of FeNi nanocompounds

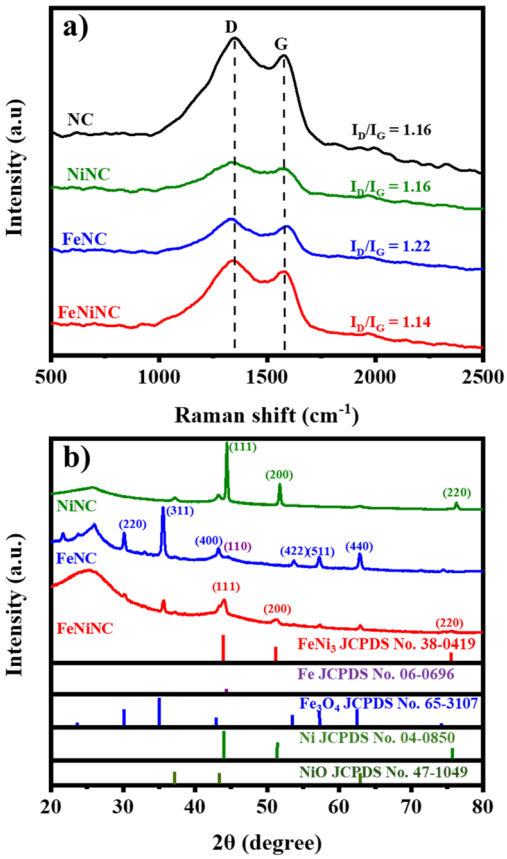

Fig. 2 (a) Raman spectra of the NC precursor formed at 700 °C, and FeNC, NiNC and FeNiNC catalysts; (b) XRD pattern of FeNC, NiNC and FeNiNC catalysts.

with an average particle diameter of approximately 15 nm, a value consistent with previous reports.[46] Furthermore, EDX analysis indicated that the alloy is slightly Ni-rich, containing 38.27 wt% Fe and 61.73 wt% Ni, corresponding to an approximate atomic ratio of 1 : 1.5.

Electrochemical characterization

The electrocatalytic performance of the prepared catalysts towards the ORR and OER was investigated through LSV. Prior to this, CVs were conducted in N_2- and O_2- saturated 0.1 M KOH solution to activate the electrode within the potential (E) range from −0.1 to 1.6 V *vs.* RHE (Fig. 3). Enhanced current density in the OER region is observed for FeNiNC, regardless of the type of gas saturating the electrolyte. In contrast, in the ORR region, no peaks were detected in N_2-saturated 0.1 M KOH for FeNC, NiNC and FeNiNC (broken lines in Fig. 3). When the electrolyte was saturated with oxygen, a well-defined reduction peak can be seen for all samples demonstrating the occurrence of the ORR at the surface of the catalysts.

To investigate the bifunctional performance of the catalysts, LSV-RDE measurements were recorded in O_2- saturated 0.1 M KOH solution within a potential range first from 1.2 to 0.2 V *vs.* RHE for the ORR and then from 1.2 to 1.76 V *vs.* RHE for the OER (Fig. 4a). The overall catalytic activity is commonly

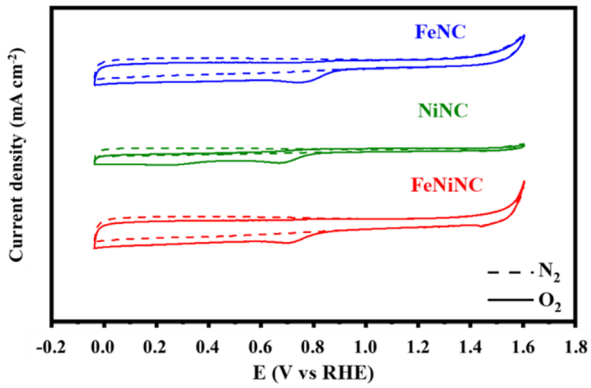

Fig. 3 CV of FeNC, NiNC and FeNiNC catalysts at a 10 mV s^{-1} scan rate.

evaluated based on the voltage gap (ΔE) between the potential at a current density of 10 mA cm^{-2} (E_{J10}) for the OER and the half-wave potential ($E_{1/2}$) for the ORR from the polarization curves of the catalysts.[47,48]

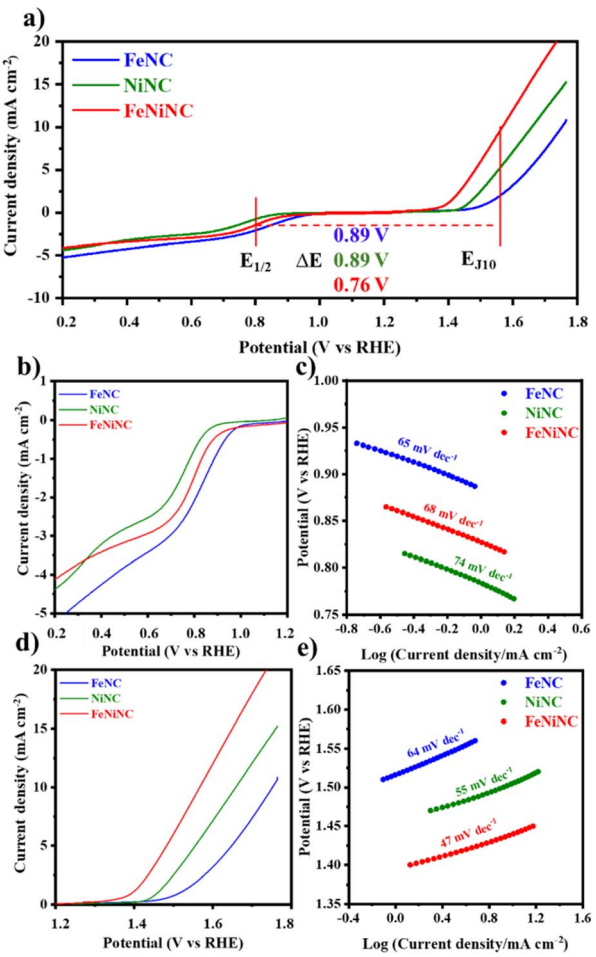

Fig. 4 LSV with an RDE at a scan rate of 10 mV s^{-1} and rotation speed of 1600 rpm in O_2-saturated (0.1 M) KOH electrolyte: (a) overall LSV polarization curve, (b) LSV curve for the ORR and (c) corresponding Tafel plots, (d) LSV curves for the OER and (e) corresponding Tafel plot of FeNC (blue), NiNC (green) and FeNiNC catalysts (red).

According to this approach, Fig. 4a indicates the FeNiNC catalyst has the best bifunctional activity. Its ΔE value of 0.76 V is much lower than those of FeNC (0.89 V) and NiNC (0.89 V). Fig. 4b shows the ORR activity of all catalysts, evidencing the half-potential for FeNiNC (0.81 V) to be intermediate between those of FeNC (0.86 V) and NiNC (0.77 V). The Tafel plots of the catalysts towards the ORR, realized plotting the half-wave potential values *versus* the logarithm of the current density, are reported in Fig. 4c. Their linear fit shows the lowest slope, *i.e.*, the fastest reaction kinetics, for FeNC (65 mV dec^{-1}) followed by FeNiNC and NiNC (68 and 74 mV dec^{-1}, respectively).

Fig. 4d shows the OER activity of the FeNiNC (1.57 V) electrocatalyst to be substantially better than those of FeNC (1.75 V) and NiNC (1.66 V). Concerning the OER activity, the overpotential (η) at 10 mA cm^{-2} of FeNiNC is 340 mV (Fig. 4d), which is much lower than those of NiNC ($\eta = 430$ mV) and FeNC ($\eta = 520$ mV), indicating that the iron–nickel alloy plays a vital role as the catalytic active site for the oxygen evolution reaction. The incorporation of Fe into Ni alters the 3d orbital band structure of the latter, enlarging metal-O covalency, which promotes electron transfer between the metal cation and O adsorbates. This facilitates the extraction of electrons from oxygen, thereby accelerating the OER process.[48] In Fig. 4e, the Tafel slope of FeNiNC is 47 mV dec^{-1}, being smaller than those of NiNC (55 mV dec^{-1}) and FeNC (64 mV dec^{-1}), indicating fast kinetics for the OER of FeNiNC.

The obtained ΔE values are compared in Table 1 with those previously reported in the literature, showing FeNiNC has a bifunctional OER/ORR activity comparable to or even better than that of other Fe and Ni based catalysts. The dual-metal active sites of Fe and Ni promote efficient adsorption and activation of oxygen intermediates during the OER, although they slightly weaken oxygen binding during the ORR, resulting in a minor decrease in $E_{1/2}$ for FeNiNC. In SWBs, both the OER and ORR are critical due to their sluggish kinetics,[54–56] and the OER competes with the chlorine evolution reaction (CER), making OER selectivity essential for safe and efficient battery operation. Therefore, catalysts for SWBs are expected to exhibit well-balanced OER and ORR activities. Accordingly, SWBs were assembled (see Fig. 5) using FeNiNC with the lowest ΔE and compared to those with the benchmark Pt/C-RuO_2.

Table 1 Comparison of the bifunctional performance of FeNiNC electrocatalysts

Catalysts	ORR $E_{1/2}$ (V *vs.* RHE)	OER E_{J10} (V *vs.* RHE)	ΔE (V)	Ref.
FeNiSAs/NC	0.88	1.64	0.76	49
Fe-NiNC-50	0.88	1.62	0.73	50
FeNi-NC	0.85	1.59	0.74	51
FeNi@C/NG	0.84	1.66	0.82	52
FeNi/NS-C	0.83	1.58	0.75	53
FeNiNC	0.81	1.57	0.76	This work
FeNC	0.86	1.75	0.89	This work
NiNC	0.77	1.66	0.89	This work

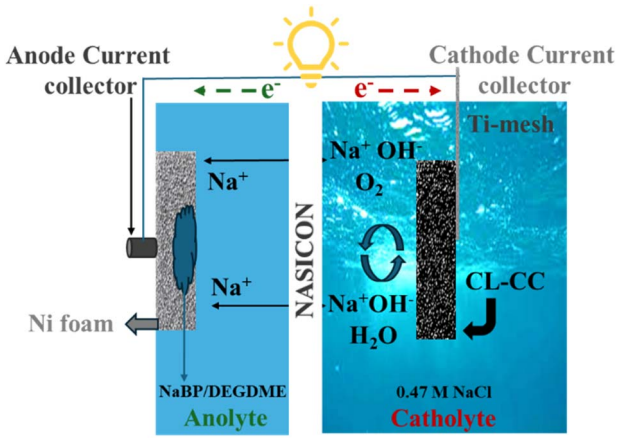

Fig. 5 Schematic illustration of the cell setup for a seawater battery employing the NaBP/DEGDME solution as an anolyte and 0.47 M NaCl as a catholyte. CL-CC is catalyst-loaded carbon cloth.

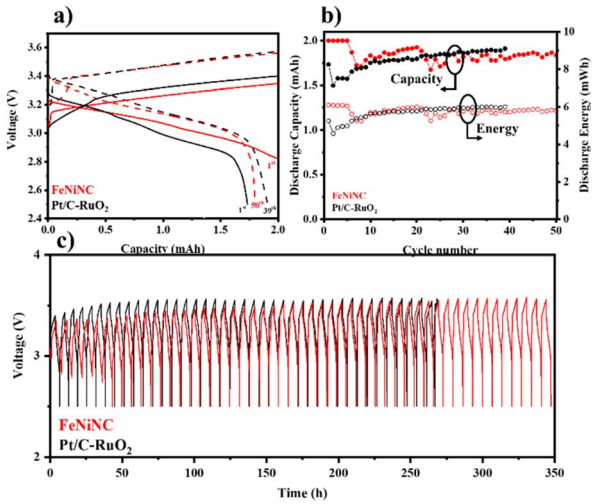

Fig. 6 Galvanostatic charge–discharge of SWBs using both Pt/C-RuO_2 and FeNiNC as electrocatalysts at 0.3 mA cm^{-2}, up to 2 mAh: (a) voltage profiles at the 1st and 38th cycles, (b) discharge specific capacity with the discharge energy and (c) long cycling time.

Performance of seawater batteries

The charge–discharge voltage profiles for the cell galvanostatically cycled at a current density of 0.3 mA cm^{-2} are presented in Fig. 6a. The cells were charged either up to 2 mA h or 4.0 V and discharged down to 2 mA h or 2.5 V. The solid line represents the 1st cycle, while the dashed line corresponds to the last recorded cycle. The same analysis was performed using bare CC as the cathode. As shown in Fig. S4, the SWB with bare CC exhibits a significantly higher overpotential compared to the cells employing electrocatalyst-modified CC, confirming the critical role of the catalyst in enhancing cell efficiency. In both Fig. 6a and S4, during the first charge, Na^+ ions transfer from seawater to the anolyte through the NASICON separator, finally plating on the Ni foam current collector. From the 2nd cycle onward, the voltage profile changes since Na-BP undergoes desodiation during discharge. Therefore, sodiation of BP becomes evident as an additional voltage plateau at 3.15 V, in addition to the plateau due to Na plating observed at 3.4 V.

Upon the initial discharge, corresponding to Na stripping and Na-BP desodiation, the FeNiNC-based cell delivers a capacity of 2.0 mA h with a final discharge potential of 2.8 V. Although full discharge was obtained in the first five cycles, the discharge capacity became irregular in the later cycles. This instability could result from catalyst corrosion induced by Cl^- ions and/or issues in the experimental setup, such as water circulation or fluctuations in dissolved oxygen content. However, in any case, SWB cycling was feasible throughout 50 cycles, and the FeNiNC-based seawater battery retains 90.7% of its initial capacity, accompanied by a gradual decrease in discharge voltage. In contrast, the Pt/C–RuO_2 cell delivers a discharge capacity of 1.75 mA h due to the 2.5 V cut-off (Fig. 6a). During cycling, the discharge capacity increases (Fig. 6b); however, it never reaches 2.0 mA h because of the higher overpotential. In the same figure, the discharge energy output of the SWBs is also presented. During cycles 10–20, although the SWBs with FeNiNC show a slightly lower discharge capacity than those with Pt/C–RuO_2, the energy output is comparable, indicating the low overpotential of the SWBs with FeNiNC.

Fig. 6c shows the time–voltage profiles of the SWB cells that featured FeNiNC and Pt/C-RuO_2 as the electrocatalysts; the former cell shows an overpotential increase during the first several cycles to acquire the same profile as Pt/C-RuO_2. In the case of the cell with FeNiNC, stable cycling was possible until 50 cycles (equivalent to 350 h), indicating good performance stability.

Conclusions

A bifunctional catalyst, composed of FeNi alloys on a functionalized carbon support, prepared from urea and a biochar derived from hazelnut shells, exhibited excellent ORR–OER activity. A low differential potential of 0.76 V, between the half-potential for the ORR and the potential where current density is equal to 10 mA cm^{-2} for the OER, was achieved. The FeNiNC electrocatalyst was successfully integrated into the cathode of SWBs, with a NaBP/DEGDME anolyte, yielding promising results. Notably, the proposed catalyst material allowed enhanced long-term stability and durability of SWBs, compared to a commercial PGM catalyst, maintaining performance for over 350 hours at 0.3 mA cm^{-2}.

Author contributions

Conceptualization, M. A. N. and S. P.; methodology, P. P. M. P., J. M. and M. A. N.; validation, A. T. and M. A. N.; formal analysis, P. P. M. P., A. T., and J. M.; investigation, P. P. M. P., A. K., J. M. and M. A. N.; resources, M. A. N.; data curation, P. P. M. P. and A. K.; writing—original draft preparation, P. P. M. P. and J. M.; writing—review and editing, A. T., S. P., and M. A. N.; supervision, M. A. N.; project administration, M. A. N.; funding

acquisition, M. A. N. All authors have read and agreed to the published version of the manuscript.

Conflicts of interest

The authors declare no conflicts of interest.

Data availability

The data supporting this article have been included as part of the supplementary information (SI). Supplementary information is available. See DOI: https://doi.org/10.1039/d5se00907c.

Acknowledgements

This work was developed in the framework of the project SBAM (Stoccaggio di energia con Batterie ad Acqua di Mare), CUP B87H21012170003, funded by MiTE-CSEA within the PTR (Piano Triennale di Realizzazione) 2019–2021 of the national RSE (Ricerca di Sistema Elettrico). A. T. acknowledges financial support from the Sapienza University of Rome for the project "Catalysts for multifunctional SeaWater Batteries (C4SWB)" in the framework of ATENEO 2023 Progetti Medi (no. RM123188F7C37868).

References

1 Y. Kim, W.-G. Lee, Secondary Seawater Batteries, *Seawater Batteries: Principles, Materials and Technology*, 2022, pp. 91–293, DOI: 10.1007/978-981-19-0797-5_3.

2 S. M. Hwang, J. S. Park, Y. Kim, W. Go, J. Han, Y. Kim and Y. Kim, Rechargeable Seawater Batteries—From Concept to Applications, *Adv. Mater.*, 2019, **31**, 1804936, DOI: 10.1002/adma.201804936.

3 M. Abirami, S. M. Hwang, J. Yang, S. T. Senthilkumar, J. Kim, W. S. Go, B. Senthilkumar, H. K. Song and Y. Kim, A Metal-Organic Framework Derived Porous Cobalt Manganese Oxide Bifunctional Electrocatalyst for Hybrid Na-Air/Seawater Batteries, *ACS Appl. Mater. Interfaces*, 2016, **8**, 32778–32787, DOI: 10.1021/acsami.6b10082.

4 W. Go, J. Kim, J. Pyo, J. B. Wolfenstine and Y. Kim, Investigation on the Structure and Properties of $Na_{3.1}Zr_{1.55}Si_{2.3}P_{0.7}O_{11}$as a Solid Electrolyte and Its Application in a Seawater Battery, *ACS Appl. Mater. Interfaces*, 2021, **13**, 52727–52735, DOI: 10.1021/acsami.1c17338.

5 W. da S. Freitas, P. P. M. Pico, A. D'epifanio and B. Mecheri, Nanostructured Fe-N-C as Bifunctional Catalysts for Oxygen Reduction and Hydrogen Evolution, *Catalysts*, 2021, **11**(12), 1525, DOI: 10.3390/catal11121525.

6 A. R. C. Bredar, M. D. Blanchet, A. R. Burton, B. E. Matthews, S. R. Spurgeon, R. B. Comes and B. H. Farnum, Oxygen Reduction Electrocatalysis with Epitaxially Grown Spinel $MnFe_2O_4$ and Fe_3O_4, *ACS Catal.*, 2022, **12**, 3577–3588, DOI: 10.1021/acscatal.1c05172.

7 S. Macchi, I. Denmark, T. Le, M. Forson, M. Bashiru, A. Jalihal and N. Siraj, Recent Advancements in the Synthesis and Application of Carbon-Based Catalysts in the ORR, *Electrochem*, 2022, **3**, 1–27, DOI: 10.3390/electrochem3010001.

8 R. Meng, C. Zhang, Z. Lu, X. Xie, Y. Liu, Q. Tang, H. Li, D. Kong, C. N. Geng, Y. Jiao, Z. Fan, Q. He, Y. Guo, G. Ling and Q. H. Yang, An Oxygenophilic Atomic Dispersed Fe-N-C Catalyst for Lean-Oxygen Seawater Batteries, *Adv. Energy Mater.*, 2021, **11**(23), 2100683, DOI: 10.1002/aenm.202100683.

9 J.-W. Zhao, Y. Li, D. Luan, W. Xiong and D. Lou, Structural Evolution and Catalytic Mechanisms of Perovskite Oxides in Electrocatalysis, *Sci. Adv.*, 2024, **10**, eadq4696, DOI: 10.3390/catal11121525.

10 H. F. Wang, L. Chen, H. Pang, S. Kaskel and Q. Xu, MOF-Derived Electrocatalysts for Oxygen Reduction, Oxygen Evolution and Hydrogen Evolution Reactions, *Chem. Soc. Rev.*, 2020, **49**, 1414–1448, DOI: 10.1039/C9CS00906J.

11 Y. Zhao, D. P. Adiyeri Saseendran, C. Huang, C. A. Triana, W. R. Marks, H. Chen, H. Zhao and G. R. Patzke, Oxygen Evolution/Reduction Reaction Catalysts: From In Situ Monitoring and Reaction Mechanisms to Rational Design, *Chem. Rev.*, 2023, **123**, 6257–6358, DOI: 10.1021/acs.chemrev.2c00515.

12 M. Wang, Y. Wang, S. S. Mao and S. Shen, Transition-Metal Alloy Electrocatalysts with Active Sites Modulated by Metal-Carbide Heterophases for Efficient Oxygen Evolution, *Nano Energy*, 2021, **88**, 106216, DOI: 10.1016/j.nanoen.2021.106216.

13 S. Dresp, F. Dionigi, M. Klingenhof, T. Merzdorf, H. Schmies, J. Drnec, A. Poulain and P. Strasser, Molecular Understanding of the Impact of Saline Contaminants and Alkaline PH on NiFe Layered Double Hydroxide Oxygen Evolution Catalysts, *ACS Catal.*, 2021, **11**, 6800–6809, DOI: 10.1021/acscatal.1c00773.

14 S. Jin, Are Metal Chalcogenides, Nitrides, and Phosphides Oxygen Evolution Catalysts or Bifunctional Catalysts?, *ACS Energy Lett.*, 2017, **2**, 1937–1938, DOI: 10.1021/acsenergylett.7b00679.

15 X. Hu, R. Wang, W. Feng, C. Xu and Z. Wei, Electrocatalytic Oxygen Evolution Activities of Metal Chalcogenides and Phosphides: Fundamentals, Origins, and Future Strategies, *J. Energy Chem.*, 2023, **81**, 167–191, DOI: 10.1016/j.jechem.2023.01.062.

16 K. Artyushkova, A. Serov, S. Rojas-Carbonell and P. Atanassov, Chemistry of Multitudinous Active Sites for Oxygen Reduction Reaction in Transition Metal-Nitrogen-Carbon Electrocatalysts, *J. Phys. Chem. C*, 2015, **119**, 25917–25928, DOI: 10.1021/acs.jpcc.5b07653.

17 W. da Silva Freitas, A. D'Epifanio, C. Lo Vecchio, I. Gatto, V. Baglio, V. C. A. Ficca, E. Placidi and B. Mecheri, Tailoring MOF Structure via Iron Decoration to Enhance ORR in Alkaline Polymer Electrolyte Membrane Fuel Cells, *Chem. Eng. J.*, 2023, **465**, 142987, DOI: 10.1016/j.cej.2023.142987.

18 M. Aysla Costa De Oliveira, A. D'Epifanio, H. Ohnuki and B. Mecheri, Platinum Group Metal-Free Catalysts for Oxygen Reduction Reaction: Applications in Microbial Fuel

Cells, *Catalysts*, 2020, **10**(5), 475, DOI: 10.3390/catal10050475.

19 M. A. C. de Oliveira, V. C. A. Ficca, R. Gokhale, C. Santoro, B. Mecheri, A. D'Epifanio, S. Licoccia and P. Atanassov, Iron(II) Phthalocyanine (FePc) over Carbon Support for Oxygen Reduction Reaction Electrocatalysts Operating in Alkaline Electrolyte, *J. Solid State Electrochem.*, 2021, **25**, 93–104, DOI: 10.1007/s10008-020-04537-x.

20 S. Zhang, H. Zhang, X. Hua and S. Chen, Tailoring Molecular Architectures of Fe Phthalocyanine on Nanocarbon Supports for High Oxygen Reduction Performance, *J. Mater. Chem. A*, 2015, **3**, 10013–10019, DOI: 10.1039/c5ta01400j.

21 T. Taniguchi, H. Tateishi, S. Miyamoto, K. Hatakeyama, C. Ogata, A. Funatsu, S. Hayami, Y. Makinose, N. Matsushita, M. Koinuma, *et al.*, A Self-Assembly Route to an Iron Phthalocyanine/Reduced Graphene Oxide Hybrid Electrocatalyst Affording an Ultrafast Oxygen Reduction Reaction, *Part. Part. Syst. Charact.*, 2013, **30**, 1063–1070, DOI: 10.1002/ppsc.201300177.

22 L. Osmieri, A. H. A. Monteverde Videla, P. Ocón and S. Specchia, Kinetics of Oxygen Electroreduction on Me-N-C (Me = Fe, Co, Cu) Catalysts in Acidic Medium: Insights on the Effect of the Transition Metal, *J. Phys. Chem. C*, 2017, **121**, 17796–17817, DOI: 10.1021/acs.jpcc.7b02455.

23 C. Chen, M. Sun, F. Zhang, H. Li, M. Sun, P. Fang, T. Song, W. Chen, J. Dong, B. Rosen, *et al.*, Adjacent Fe Site Boosts Electrocatalytic Oxygen Evolution at Co Site in Single-Atom-Catalyst through a Dual-Metal-Site Design, *Energy Environ. Sci.*, 2023, **16**, 1685–1696, DOI: 10.1039/d2ee03930c.

24 C. Streb, Z. Chen, W. Cheng, K. Cao, J. Meng, S. Rahali, E. Ebrahimi, S. A. Chala, N. Ma, R. Liu, K. Lakshmanan, C.-C. Cheung, C.-Y. Chang, H. Luo, Y. Wang and B. J. Hwang, A Bifunctional Iron-Nickel Oxygen Reduction / Oxygen Evolution Catalyst for High-Performance Rechargeable Zinc-Air Batteries, *Small*, 2025, **21**, 2409161, DOI: 10.26434/chemrxiv-2024-d4885.

25 X. Zhu, D. Zhang, C. J. Chen, Q. Zhang, R. S. Liu, Z. Xia, L. Dai, R. Amal and X. Lu, Harnessing the interplay of Fe–Ni atom pairs embedded in nitrogen-doped carbon for bifunctional oxygen electrocatalysis, *Nano Energy*, 2020, **71**, 104597, DOI: 10.1016/j.nanoen.2020.104597.

26 X. Wu, Z. Yang, C. Li, S. Shao, G. Qin and X. Meng, Organizational and Mechanistic Modulation of ORR/OER Activity in M1M2-N-C Bimetallic Catalysts, *ACS Catal.*, 2025, **15**(1), 432–446, DOI: 10.1021/acscatal.4c06280.

27 W. Gao, Z. Lin, H. Chen, S. Yan, Y. Huang, X. Hu and S. Zhang, A Review on N-Doped Biochar for Enhanced Water Treatment and Emerging Applications, *Fuel Process. Technol.*, 2022, **237**, 107468, DOI: 10.1016/j.fuproc.2022.107468.

28 G. Hou, J. Wu, T. Li, J. Lin, B. Wang, L. Peng, T. Yan, L. Hao, L. Qiao and X. Wu, Nitrogen-Rich Biomass Derived Three-Dimensional Porous Structure Captures FeNi Metal Nanospheres: An Effective Electrocatalyst for Oxygen Evolution Reaction, *Int. J. Hydrogen Energy*, 2022, **47**, 12487–12499, DOI: 10.1016/j.ijhydene.2022.02.004.

29 Y. Kim, J. K. Kim, C. Vaalma, G. H. Bae, G. T. Kim, S. Passerini and Y. Kim, Optimized Hard Carbon Derived from Starch for Rechargeable Seawater Batteries, *Carbon*, 2018, **129**, 564–571, DOI: 10.1016/j.carbon.2017.12.059.

30 S. Susanto, T. Nurtono, W. Widiyastuti, M. H. Yeh and H. Setyawan, Controlling N-Doping Nature at Carbon Aerogels from Biomass for Enhanced Oxygen Reduction in Seawater Batteries, *ACS Omega*, 2024, **9**, 13994–14004, DOI: 10.1021/acsomega.3c09297.

31 B. Wang, Y. Wang, Y. Peng, X. Wang, N. Wang, J. Wang and J. Zhao, Nitrogen-Doped Biomass-Based Hierarchical Porous Carbon with Large Mesoporous Volume for Application in Energy Storage, *Chem. Eng. J.*, 2018, **348**, 850–859, DOI: 10.1016/j.cej.2018.05.061.

32 A. Beda, J.-M. Le Meins, P.-L. Taberna, P. Simon and C. Matei Ghimbeu, Impact of Biomass Inorganic Impurities on Hard Carbon Properties and Performance in Na-Ion Batteries, *Sustainable Mater. Technol.*, 2020, **26**, e00227, DOI: 10.1016/j.susmat.2020.e00227.

33 X. Liu, X. Yang, Z. Zhao, T. Fang, K. Yi, L. Chen, S. Liu, R. Wang and X. Jia, Isolated Binary Fe-Ni Metal-Nitrogen Sites Anchored on Porous Carbon Nanosheets for Efficient Oxygen Electrocatalysis through High-Temperature Gas-Migration Strategy, *ACS Appl. Mater. Interfaces*, 2024, **16**, 18703–18712, DOI: 10.1021/acsami.3c17193.

34 R. Z. Snitkoff-Sol, Y. Presman and L. Elbaz, Investigating the Fuel Cell Performance Tradeoffs of Thick Catalyst Layers, *ChemElectroChem*, 2025, **12**(10), e202500038, DOI: 10.1002/celc.202500038.

35 J. Luo, Y. Yi and Z. Fang, Nitrogen-rich magnetic biochar prepared by urea was used as an efficient catalyst to activate persulfate to degrade organic pollutants, *Chemosphere*, 2023, **339**, 139614, DOI: 10.1016/j.chemosphere.2023.139614.

36 C. Zhao, L. Ge, X. Li, M. Zuo, C. Xu, S. Chen, Q. Li, Y. Wang and C. Xu, Effects of the carbonization temperature and intermediate cooling mode on the properties of coal-based activated carbon, *Energy*, 2023, **273**, 127177, DOI: 10.1016/j.energy.2023.127177.

37 H. Li, W. Kang, L. Wang, Q. Yue, S. Xu, H. Wang and J. Liu, Synthesis of three-dimensional flowerlike nitrogen-doped carbons by a copyrolysis route and the effect of nitrogen species on the electrocatalytic activity in oxygen reduction reaction, *Carbon*, 2013, **54**, 249–257, DOI: 10.1016/j.carbon.2012.11.036.

38 W. Barszcz, M. Łożyńska and J. Molenda, Impact of pyrolysis process conditions on the structure of biochar obtained from apple waste, *Sci. Rep.*, 2024, **14**(1), 10501, DOI: 10.1038/s41598-024-61394-8.

39 D. Ma, Y. Zhang, M. Liang, R. Niu, Y. Ge, Y. Zou and X. Dong, Effect of the Microstructure of Carbon Supports on the Oxygen Reduction Properties of the Loaded Non-Noble Metal Catalysts, *Nanomaterials*, 2025, **15**(17), 1327, DOI: 10.3390/nano15171327.

40 W. Chen, Y. Chen, H. Yang, K. Li, X. Chen and H. Chen, Investigation on biomass nitrogen-enriched pyrolysis:

Influence of temperature, *Bioresour. Technol.*, 2018, **249**, 247–253, DOI: 10.1016/j.biortech.2017.10.022.

41 B. Clair, J. Ruelle and J. Beauchene, Mesoporosity as a new parameter for understanding tension stress generation in trees, *J. Exp. Bot.*, 2009, **60**(11), 3023–3030, DOI: 10.1093/jxp/erp133.

42 D. S. Yuan, T. X. Zhou, S. L. Zhou, W. J. Zou, S. S. Mo and N. N. Xia, Nitrogen-enriched carbon nanowires from the direct carbonization of polyaniline nanowires and its electrochemical properties, *Electrochem. Commun.*, 2011, **13**(3), 242–246, DOI: 10.1016/j.elecom.2010.12.023.

43 S. Ren, X. Tang, P. Zhang, W. Peng, X. Zeng, H. Zheng and Z. Wan, Multi-scale porous nitrogen-rich large carbon networks modified by bimetallic FeNi alloys as exceptional bifunctional catalysts for rechargeable Zn-air batteries, *J. Energy Storage.*, 2025, **105**, 114740, DOI: 10.1016/j.est.2024.114740.

44 S. Deng, X. Han, N. Lv, X. Yang, Q. Liu, Y. Jiang, Y. Yang and B. Xi, Unveiling the Activation Mechanism: The Role of Nitrogen-Doped Biochar in Enhancing Fe(VI) Catalysis, *Chem. Eng. J.*, 2024, **486**, 150263, DOI: 10.1016/j.cej.2024.150263.

45 Y. Wang, W. Nong, N. Gong, T. Salim, M. Luo, T. L. Tan, K. Hippalgaonkar, Z. Liu and Y. Huang, Tuning Electronic Structure and Composition of FeNi Nanoalloys for Enhanced Oxygen Evolution Electrocatalysis via a General Synthesis Strategy, *Small*, 2022, **18**(41), 2203340, DOI: 10.1002/smll.202203340.

46 N. F. el Boraei, M. A. M. Ibrahim and M. A. Naghmash, Nanocrystalline FeNi alloy powder prepared by electrolytic synthesis; characterization and its high efficiency in removing Remazol Red dye from aqueous solution, *J. Phys. Chem. Solids*, 2022, **167**, 110714, DOI: 10.1016/j.jpcs.2022.110714.

47 Z. Chen, J. Zeng, X. Dong, Z. Liu, J. Wang and Q. Zhong, The enhanced fast-charging and cycle stability for high energy efficiency KI-assisted rechargeable zinc-air batteries, *J. Power Sources*, 2025, **646**, 237286, DOI: 10.1016/j.jpowsour.2025.237286.

48 X. Wu, C. Tang, Y. Cheng, X. Min, S. P. Jiang and S. Wang, Bifunctional Catalysts for Reversible Oxygen Evolution Reaction and Oxygen Reduction Reaction, *Chem.–Eur. J.*, 2020, **26**(18), 3906–3929, DOI: 10.1002/chem.201905346.

49 M. Gopalakrishnan, W. Kao-Ian, M. Rittiruam, S. Praserthdam, P. Praserthdam, W. Limphirat, M. T. Nguyen, T. Yonezawa and S. Kheawhom, 3D Hierarchical MOF-Derived Defect-Rich NiFe Spinel Ferrite as a Highly Efficient Electrocatalyst for Oxygen Redox Reactions in Zinc-Air Batteries, *ACS Appl. Mater. Interfaces.*, 2024, **16**(9), 11537–11551, DOI: 10.1021/acsami.3c17789.

50 X. Zhu, D. Zhang, C.-J. Chen, Q. Zhang, R.-S. Liu, Z. Xia, L. Dai, R. Amal and X. Lu, Harnessing the Interplay of Fe–Ni Atom Pairs Embedded in Nitrogen-Doped Carbon for Bifunctional Oxygen Electrocatalysis, *Nano Energy*, 2020, **71**, 104597, DOI: 10.1016/j.nanoen.2020.104597.

51 C. Liu, S. Wu, S. Tian, J. Yang, J. Li, Q. Guan, F. Yin, X. Xiang, Y. Wang, X. Meng, *et al.*, Structurally Optimized Rosette-like Microspheres Carbon with Fe-Ni Single Atom Sites for Bifunctional Oxygen Electrocatalysis in Zinc-Air Batteries, *Chem. Eng. J.*, 2024, **497**, 154963, DOI: 10.1016/j.cej.2024.154963.

52 G. L. Li, B. B. Yang, X. C. Xu, S. Cao, Y. Shi, Y. Yan, X. Song and C. Hao, FeNi Alloy Nanoparticles Encapsulated in Carbon Shells Supported on N-Doped Graphene-Like Carbon as Efficient and Stable Bifunctional Oxygen Electrocatalysts, *Chem.—Eur. J.*, 2020, **26**, 2890–2896, DOI: 10.1002/chem.201904685.

53 J. ai, X. Hao, Z. Bian, Y. Wu, C. Wei, X. Yin, B. Liu, M. Fang, Y. Lv, Y. Xie, *et al.*, Elucidating the Discrepancy between the Intrinsic Structural Instability and the Apparent Catalytic Steadiness of M-N-C Catalysts toward Oxygen Evolution Reaction, *Angew. Chem., Int. Ed.*, 2024, **63**, e202409079, DOI: 10.1002/anie.202409079.

54 T. Huang, M. Guo, W. Li, Y. Bao, A. Yu, D. S. Li, J. Tu, M. Wang, W. Hao and C. Sun, High-performance oxygen evolution reaction via self-optimizing interface engineering with simultaneous activation of dual-sites of surface oxyhydroxides, *Appl. Surf. Sci.*, 2024, **659**, 159936, DOI: 10.1016/j.apsusc.2024.159936.

55 J. Wu, R. Chong, Z. Li, S. Xu, Y. Liu, X. He, J. Qian, J. Zhang, L. Wang and Z. H. Zhang, Tailoring Active Sites in Amorphous NiFe-MOFs through Pyridine Ligand Coordination for Enhanced Oxygen Evolution Performance, *ACS Appl. Mater. Interfaces*, 2025, **17**(37), 52297–52306, DOI: 10.1021/acsami.5c14277.

56 S. Arnold, L. Wang and V. Presser, Dual-Use of Seawater Batteries for Energy Storage and Water Desalination, *Small*, 2022, **18**(43), 2107913, DOI: 10.1002/smll.202107913.